IOPscience iopscience.iop.org

Home Search Collections Journals About Contact us My IOPscience

Nitric oxide PLIF measurement in a point-to-plane pulsed discharge in vitiated air of a propane/air flame

This content has been downloaded from IOPscience. Please scroll down to see the full text.

2014 Plasma Sources Sci. Technol. 23 065005

(http://iopscience.iop.org/0963-0252/23/6/065005)

View the table of contents for this issue, or go to the journal homepage for more

Download details:

IP Address: 132.174.255.176
This content was downloaded on 01/06/2015 at 13:22

Please note that terms and conditions apply.

IOP Publishing Plasma Sources Science and Technology

Plasma Sources Sci. Technol. 23 (2014) 065005 (11pp) doi:10.1088/0963-0252/23/6/065005

Nitric oxide PLIF measurement in a point-to-plane pulsed discharge in vitiated air of a propane/air flame

J B Schmidt[1], N Jiang[1] and B N Ganguly[2]

[1] Spectral Energies, LLC, Dayton OH 45433, USA
[2] Air Force Research Laboratory, WPAFB OH 45433, USA

E-mail: JSchmidt@SpectralEnergies.com

Received 20 February 2014, revised 23 June 2014
Accepted for publication 15 July 2014
Published 18 August 2014

Abstract

The effect of a point-to-plane pulsed discharge on the vitiated downstream of a propane/air flame has been investigated by phase-locked NO planar laser-induced-fluorescence (PLIF) measurements. Phase-locked NO PLIF measurements with the variation of pulsed plasma energy, equivalence ratio and applied voltage rise time have been performed. Fast rise time (25 ns) and slower rise time (150 ns) high-voltage pulsers are used to produce NO radical densities greater than the ambient flame-produced NO radicals in lean, balanced and rich premixed flames. The pulsed plasma produced excess NO radical densities were found to decay to 50% level with time constants greater than 250 μs in the burnt gas regions with gas temperatures greater than 1000 K. The super-equilibrium NO populations were dependent on energy deposited and overall equivalence ratio, but independent of voltage pulse rise time for similar energy deposition per pulse. Due to long NO radical density decay lifetimes, super-equilibrium NO populations are convected away from production regions with the ambient flow and observed in downstream exhaust gas regions.

Keywords: Optical plasma diagnostics, Glow discharges, Plasma reactions

(Some figures may appear in colour only in the online journal)

1. Introduction

The use of plasma discharges to augment flame kinetics and enhance flame stability is an area of current research interest [1–21]. The potential impact of this study includes expanding stability limits of complex burning configurations or ultra-lean combustors, and expanding the hydrocarbon fuel base. A number of studies performed in the last decade have shown that different plasma geometries such as the corona discharge, dielectric barrier, and short repetitively pulsed discharges can affect NO (nitric oxide) production as well as other species and improve overall combustion stability. In premixed combustion, plasmas can produce reactive species from both the fuel and oxidizer stream in flame areas that otherwise have lower levels of reactive species in the low-temperature pre-heat region of a premixed, hydrocarbon flame.

Much work has also been done to determine the impact of the plasma when these reactive species are injected near the base of the premixed flame [6, 16, 17]. At this injection point, the temperature of the fuel and oxidizer streams are relatively low and have not reached the crossover temperature where combustion reactions typically occur [22]. It has been shown that when these reactive species are injected in these lower-temperature, upstream locations [8, 17], mole fractions over 0.002 can have a strong impact on flame kinetics. In this near-burner surface plasma injection configuration, a portion of the discharge volume can lie in lower temperature, lower gas conductivity regions. This reduction in conductivity can result in a smaller amount of current passed through this region for the same potential drop and discharge gap distance. For these reasons, others have modified their geometry to have the anode in the downstream gas and strike the discharge downward passing near the high temperature flame reaction zone [1, 2]. The Mini-PAC (plasma-assisted combustor) is a good example of this configuration [3, 4], however this burner configuration uses the anode as a flame stabilizer.

 © 2014 IOP Publishing Ltd Printed in the UK

Our experimental configuration specifically locates the anode outside of the flame reaction zone so that it does not act as a flame holder.

Nitric oxide is formed in non-combustion related mechanisms through non-equilibrium plasma interaction. Chemical reactions in air plasmas are initiated by electron impact on the main air constituents; N_2 and O_2. While the electron impact neutral dissociation of N_2 requires a higher minimum energy than the dissociation of O_2, both dissociative processes producing reactive atomic radicals are important for the initiation of chemical processes. Shown below in equations (1)–(5) are some of the important reactions and associated rate constants [20, 21, 24] involving N and O atoms and excited state N_2, where N_2* is any electronically excited state, including, but not limited to $N_2(A)$. It is understood that the pulsed plasma is also capable of producing many of the reactants responsible for NO generation listed in equations (1)–(5) such as $N_2(A^3\,\Sigma_u^+)$ [24], N [24], O and OH [25].

$$\mathrm{N + O} + M \leftrightarrow \mathrm{NO} + M \quad k_f = 2.7 \times 10^{-13} \tag{1}$$

$$\mathrm{N_2}\left(A^3\,\Sigma_u^+\right) + \mathrm{NO_2} \leftrightarrow \mathrm{N_2 + NO + O} \quad k_f = 1.3 \times 10^{-11} \tag{2}$$

$$\mathrm{N_2}\left(A^3\,\Sigma_u^+\right) + \mathrm{O_2} \leftrightarrow \mathrm{NO + NO} \tag{3}$$

$$\mathrm{N_2}(v' > 2) + \mathrm{O_2} \leftrightarrow \mathrm{NO + NO} \tag{4}$$

$$\mathrm{N_2} * + \mathrm{O} \leftrightarrow \mathrm{NO + N}. \tag{5}$$

Recent work has shown that even higher, electronically excited states of nitrogen (N_2 C and B states) may have a significant role in generation of NO in plasma augmented combustion [27]. While many other reaction channels may be modified by non-thermal plasmas some of these pathways are omitted here due to smaller reaction rate constants or reactant populations being sufficiently small in the applied temperature range. These involve reaction pathways involving NO_2, NO_3, N_2O, etc. All of these reactions and rates will be highly dependent on parameters such as temperature, reduced electric field and total energy deposited.

Nitric oxide can also be formed from atmospheric nitrogen gas through three hydrocarbon-combustion-related mechanisms with no fuel bound nitrogen components; thermal NO, prompt NO and the N_2O mechanisms. The thermal NO mechanism consists of three reactions shown below in equations (6)–(8) with corresponding rate coefficients [20]. This formation mechanism tends to favor high temperature gas and NO formation is considered to be unimportant at temperatures below 1800 K [22]. Prompt NO formation or the Fenimore mechanism arises from substantial NO production in the cooler, upstream portion of the premixed hydrocarbon flame that the thermal mechanism cannot predict and is shown in equations (9) and (10), assuming CH has already been formed. For equivalence ratios less than ~1.2 conversion of hydrogen cyanide (HCN) to NO follows the chain shown in equations (11)–(14). For equivalence ratios richer than 1.2 the combustion chemistry becomes more complex and other pathways to form NO become available [23, 24]. Since concentrations of O and CH increase with increasing temperature, the formation of prompt NO increases with increasing flame temperature. Formation of NO through the N_2O mechanism is shown in equations (15)–(17) and is especially important in lean equivalence ratios ($\Phi = 0.80$). Since this sequence requires the O atom and the three-body recombination reaction in equation (11), the formation of NO is favored with increasing air pressure.

$$\mathrm{N_2 + O} \leftrightarrow \mathrm{NO + N} \quad k_f = 2 \times 10^{14} e^{\left(\frac{-315}{RT}\right)} \tag{6}$$

$$\mathrm{O_2 + N} \leftrightarrow \mathrm{NO + O} \quad k_f = 6.4 \times 10^{9} e^{\left(\frac{-26}{RT}\right)} \tag{7}$$

$$\mathrm{N + OH} \leftrightarrow \mathrm{NO + H} \quad k_f = 3.8 \times 10^{13} \tag{8}$$

$$\mathrm{CH + N_2} \leftrightarrow \mathrm{HCN + N} \tag{9}$$

$$\mathrm{C + N_2} \leftrightarrow \mathrm{CN + N} \tag{10}$$

$$\mathrm{HCN + O} \leftrightarrow \mathrm{NCO + H} \tag{11}$$

$$\mathrm{NCO + H} \leftrightarrow \mathrm{NH + CO} \tag{12}$$

$$\mathrm{NH + H} \leftrightarrow \mathrm{H_2 + N} \tag{13}$$

$$\mathrm{N + OH} \leftrightarrow \mathrm{NO + H} \tag{14}$$

$$\mathrm{N_2 + O} + M \leftrightarrow \mathrm{N_2O} + M \tag{15}$$

$$\mathrm{N_2O + H} \leftrightarrow \mathrm{NO + NH} \tag{16}$$

$$\mathrm{N_2O + O} \leftrightarrow \mathrm{NO + NO}. \tag{17}$$

When a pulsed plasma is applied to a combustion event, two distinct regimes are formed to help determine the temporal evolution of the produced NO populations; the initial production dominated by plasma kinetics and the resulting decay of the produced NO dominated by combustion kinetics. This is supported by Uddi *et al* [21] where initial NO concentrations from a nanosecond duration pulse in low pressure fuel/air flows rise much faster than Zel'dovich mechanisms predict, but slower than reactions with electronically excited nitrogen atoms and molecules and decays are dominated by reverse Zel'dovich mechanisms and NO_2 reactions with ozone. These results further concluded that long lifetime N_2 and O_2 metastables dominated NO production at low pressure. The current study is focused on examining these distinct regimes, the initial level of production and the temporal decay of NO in a premixed, hydrocarbon flame to determine the impact that short-duration, repetitively pulsed, point-to-plane nanosecond plasma discharges can have on premixed hydrocarbon flame kinetics at atmospheric pressure.

2. Experimental

The experimental setup used is shown in figure 1(*a*), which closely resembles the setup used in previous work [25, 26]. The setup consists of a premixed C_3H_8/air laminar-flow burner producing an evenly distributed conical flame. The burner used is a commercial atomic absorption type (Perkin-Elmer) with a modified cylindrical (44 millimeter (mm) diameter × 50 mm) stainless-steel head. Pressed into the stainless-steel head is a bronze insert with machined orifices consisting of five concentric rings of close spaced 1 mm diameter holes. This geometry is shown in figure 1(*b*). The propane and air are

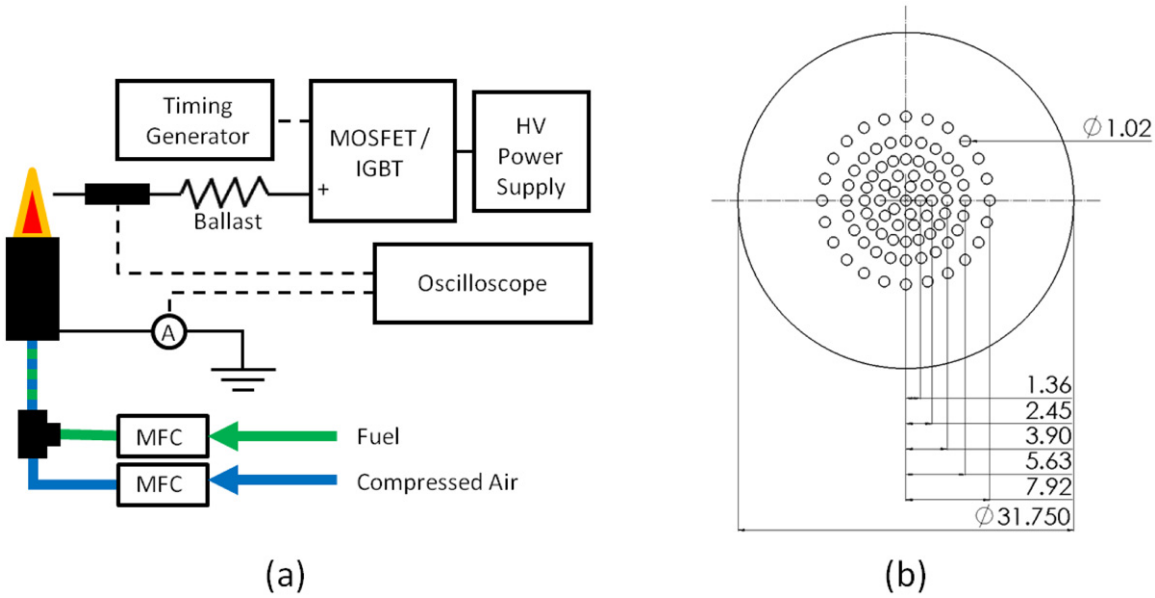

Figure 1. (*a*) Electrical and flow schematic of experimental setup. (*b*) Top view of burner geometry. Dimensions are in mm.

mixed in-line for 1 m before entering the burner section and then pass through three increasingly smaller gauge wire gauze to homogenize the mixture. Flame equivalence ratios [22] and flow speeds are accurately measured with a pair of digital thermal mass-flow controllers for both fuel and air; accurate to within 0.8% of the reading. The incoming flow speed for the conditions tested is just over 2 m per second [26]. The burner is directly grounded and an inductive Pearson probe, labeled as A in figure 1(*a*), was used for current. A 1 mm diameter molybdenum wire is suspended above the burner surface to serve as an anode for the application of the positive voltage. The thin anode tip temperature is nearly in equilibrium with the gas temperature and the soot build-up is minimal even for fuel rich flames. The pulsed voltage is varied in magnitude (up to +8 kV) and applied using a current-limiting ballast resistor at 1 kHz repetition rates. As with previous studies [25], two different high-voltage switches are used that achieve the same applied voltage levels, but with different voltage pulse rise times. The fast rise-time switch has voltage rise times near 25 nanoseconds (ns) and uses a stacked metal–oxide–semiconductor field-effect transistor (MOSFET) configuration. This is an order of magnitude faster than the slow rise-time switch which has voltage rise times near 150 ns and uses a transformer-coupled insulated-gate bipolar transistor (IGBT). The current and voltage traces were recorded for each test conditions. Figure 2 shows typical voltage and current levels for the fast rise-time switch.

Laser-induced fluorescence (LIF) theory and its applications to combustion are described in greater detail elsewhere [28–30]. NO is one of the more widely used species for planar laser-induced-fluorescence (PLIF) measurements in combustion flows. The NO molecule is chosen for this fluorescence study due to its importance in hydrocarbon/ air combustion chemistry as well as in air plasma chemistry and its advantages of being relatively stable, naturally present in flames, and its well-understood spectroscopic properties [30, 31].

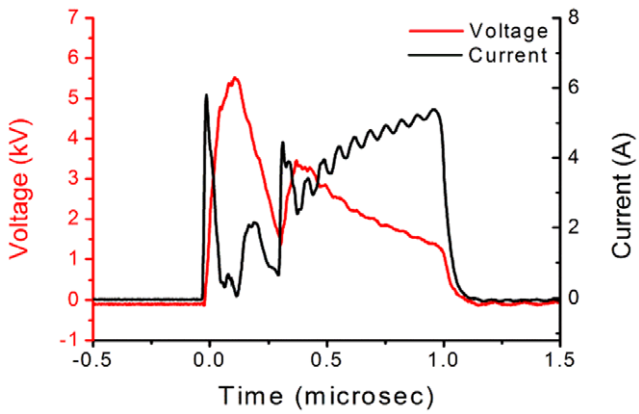

Figure 2. Typical voltage and current for tested flow conditions using the fast rise-time switch applied to a $\Phi = 1.0$ flame. +6 kV applied for 1 microsecond results in 6 A of current over 10 mm gap. Total power deposited is 15 W.

In this work we use a high-voltage discharge in a premixed, hydrocarbon flame to augment the density of flame-produced NO through normally non-existent non-equilibrium air plasma chemistry channels. Figure 3 shows a schematic of the laser diagnostic system used for the NO PLIF measurements in an atmospheric pressure burner. NO fluorescence images were acquired with a gated ICCD by exciting transitions within the $A^2\Sigma^+ \leftarrow X^2\Pi\left(v' = 0, v'' = 0\right)$ γ-band, near 226 nanometers (nm). In this band, transitions from a large range of rotational levels are easily accessible with pulsed dye lasers. The (0,0) band also has relatively strong absorption, thereby providing high fluorescence signals, while allowing for efficient rejection of laser scattering through non-resonant detection of broadband fluorescence (primarily $v'' = 0$). A dye laser (Continuum ND6000) using a combination of Sulforhodamine 640, Rhodamine 640 Perchlorate and Cresyl Violet 670 dye in a methanol solvent is pumped with the second harmonic of a 10 Hz Nd : YAG laser (Spectra-Physics PRO250)

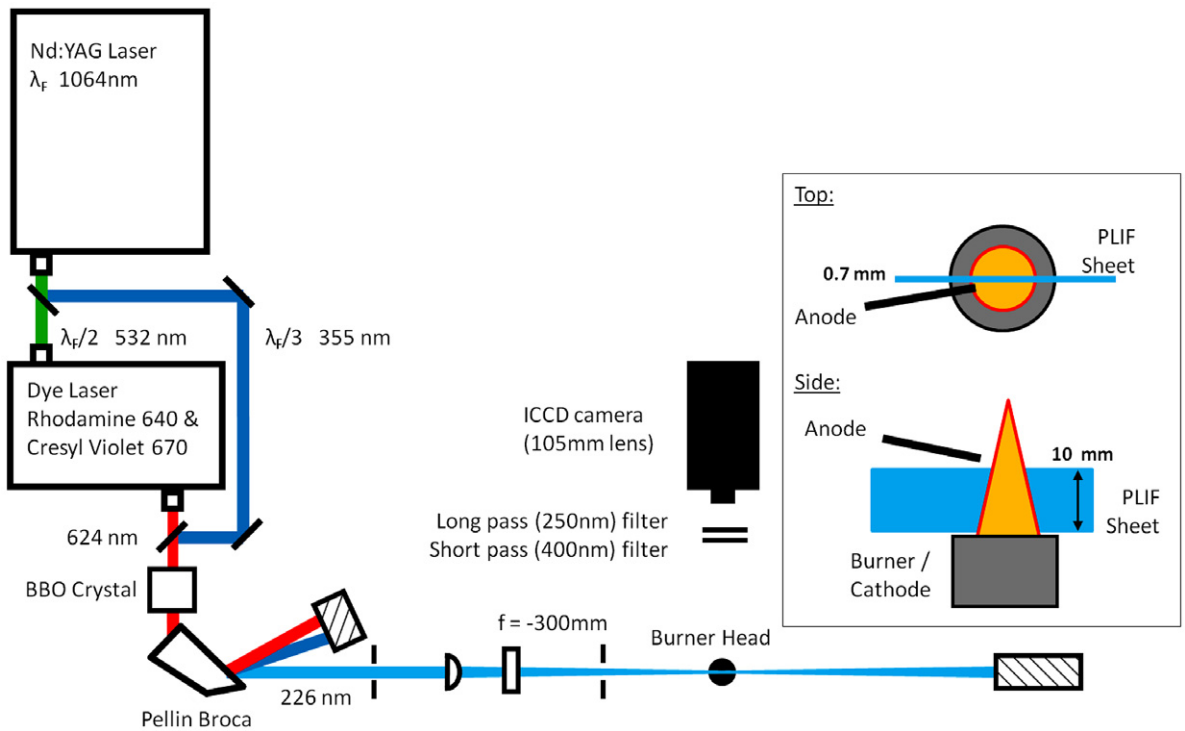

Figure 3. Laser diagnostic setup up used for NO PLIF. $A\,^2\Sigma^+ \leftarrow X\,^2\Pi$ ($v' = 0$, $v'' = 0$) γ-band, near 226 nm, is excited through frequency mixing in a BBO crystal and imaged by an ICCD with filters used to discriminate against scatter and unwanted fluorescence signal.

to produce 624 nm light. This beam is then mixed with the third harmonic from the original Spectra-Physics Nd : YAG laser inside a BBO crystal through sum frequency generation. In this configuration, over 1 mJ per pulse laser energy is produced with a measured spectral linewidth of 0.25 cm^{-1} centered near 226 nm. With this bandwidth, multiple primary rotational transitions are excited, including Q_1 14.5, 15.5, 16.5, P_1 23.5, R_1 8.5, 9.5, R_2 15.5, as well as several secondary transitions. A Pellin–Broca prism, located near the BBO crystal, is used to spectrally separate the residual dye laser and frequency-tripled YAG output from the desired UV light. The UV beam is converted into a sheet by using a $f = -300$ mm cylindrical and $f = 1000$ mm spherical lens as a single-direction telescope. This optical setup produces a UV sheet that is 0.7 mm thick and 10 mm tall within the test section. Because it is only a single direction telescope the UV sheet has a slowly diverging height. However, the rate of divergence of the beam in this direction is assumed to have negligible effects on the energy density of the sheet within the laser waist due to the long focal length of the spherical lens used.

The fluorescence signal is imaged with an ICCD camera (512×512 array) equipped with an UV $f/4.5$ lens. A 250 nm long-pass filter from Asahi and color short-pass filter from Oriel were used to block the laser scattering and unwanted fluorescence signal. The total region imaged is 17 mm by 17 mm providing a spatial resolution of 30.11 pixel per mm. The intensifier gate widths are set to provide 200 ns of uniform gating for the NO measurements, fully collecting the entire NO fluorescence decay while eliminating flame emission. The laser pulses are carefully positioned temporally to occur just after the intensifier gates are fully on, to ensure uniform gating of the fluorescence decay. A Stanford Research Systems Digital Delay Generator (DG645) is used to control timing between the laser, camera systems and the applied voltage pulses, enabling synchronization between the laser pulses, camera gates, and applied voltage.

In order to determine absolute NO concentrations, a calibration is performed by flowing a 1% NO in helium mixture through the above-mentioned burner system. Concentrations were varied through dilution with helium and total flow rates were controlled with the same mass-flow controllers mentioned previously. This configuration allows for concentrations up to 10 000 parts per million (ppm) to be calibrated and the same collection system to be used, simplifying the calibration process. Since NO populations in flame exhaust gas conditions are calibrated with known populations of NO at room temperature, corrections must be made to the above calibration to account for the thermal redistribution of rotational spectra.

Collisional quenching must be accounted for as it is a major source of reduction to quantum yield. Assuming that collisional quenching of the upper state is independent of rotational quantum number, equation (18) provides the total fluorescence signal as a function of excitation laser frequency, ν, for a broadband detector, where C_{opt} describes the total optical collection system, E_{p} is the total laser energy per pulse, A and B_i are Einstein coefficients for spontaneous emission and stimulated absorption, $f_{\mathrm{Bi}}(T)$ is the equilibrium Boltzmann fraction based on rotational/translational temperature, $Q(\chi_p, P, T)$ is the A-state quenching rate, $g_i(\mathrm{n}, \chi_{\mathrm{p}}, P, T)$ is the line shape function, and $n_{\mathrm{NO}} = \chi_{\mathrm{NO}} P / k_{\mathrm{B}} T$ is the NO number density

with χ_{NO} being the NO mole fraction. Additionally, if it is assumed that the temperature does not increase due to the nanosecond discharge, which has been shown to be the case [21], then a simplified equation relating the number density of NO during the discharge ($n_{NO,dis}$) to the collected calibration levels ($n_{NO,cal}$) is given in equation (19) and depends only on fluorescence signals (S_f) and quantum yields.

$$S_{LIF}(v) = \frac{C_{Opt} E_P A_{v'=0\to v''=2}}{\left[\sum_{v''} A_{A_{v'=0\to v''=2}} + Q\left(\chi_p, P, T\right)\right]} \times \sum_i \left\{f_{Bi}(T) B_i g_i(\nu, \chi_p, P, T)\right\} \times \chi_{NO} \frac{P}{k_B T} \tag{18}$$

$$n_{NO,dis} = \chi_{NO,cal} \frac{P}{k_B T_{cal}} \frac{S_{f,dis}}{S_{f,cal}} \times \frac{\left[\sum_{v''} A_{v'=0\to v''=2} + Q\left(\chi_p, P, T\right)\right]_{dis}}{\left[\sum_{v''} A_{v'=0\to v''=2} + Q\left(\chi_p, P, T\right)\right]_{cal}} \times \frac{\left[\sum_i f_{Bi}(T) B_i g_i(\nu, \chi_p, P, T)\right]_{cal}}{\left[\sum_i f_{Bi}(T) B_i g_i(\nu, \chi_p, P, T)\right]_{dis}} \tag{19}$$

where the total quenching rate, shown in equation (20), is given by a sum over all quenching species in the volume at those conditions.

$$Q = \sum_k n_k Q_k \tag{20}$$

This situation is complicated by the temperature gradients that are present in the 'discharge' condition. This was originally simplified by defining three zones; the pre-heat region upstream of the reaction zone, the thin reaction zone, and the exhaust region downstream of the reaction zone. However, this system is greatly simplified as the majority of the observed effects occur in the exhaust region downstream with no observed effects occurring in the pre-heat region. From this, only two regions were considered; the reaction zone and downstream exhaust products. In the reaction zone, both mole fraction and temperature depend only on equivalence ratio. In the exhaust products region, mole fraction and temperature are dependent on both equivalence ratio and distance from the reaction zone. Mole fractions and a general temperature is determined and assigned to each zone. These are determined by a global simulation conducted in CHEMKIN [32] utilizing the hydrocarbon oxidation mechanism from Lawrence Livermore National Laboratory based on a known equivalence ratio for a burner-stabilized, premixed, propane/air flame. These major quenching species include Ar, CH_4, C_2H_4, C_2H_6, CO, CO_2, He, H, H_2, H_2O, N_2, NO, N_2O, NO_2, O_2 and OH. Spontaneous radiative decay rates and collisional quenching rates were collected from the literature at a range of temperatures for similar atmospheric pressure flame conditions [21, 33–39] and equilibrium Boltzmann fraction was determined from LIFBASE [40]. The collected fluorescence images were then assigned regions based on flame structure and corrected based on the appropriate parameters for that region. Interpolation was used in the exhaust gas region to obtain a linearly varying parameter set used for correction.

Simulated NO absorption spectra generated from LIFBASE [40] is integrated over the excitation laser bandwidth for both temperature ranges. While significant vibrational temperature changes can occur within the discharge volume, this is not corrected for as the actual vibrational temperature is unknown during the discharge and will be highly spatially dependent. In this effort, the accuracy of the calibrated measurement is limited by the assumption of thermal-equilibrium population distribution. For this measurement, the error is approximately 9.4% and is largely dominated by pulse-to-pulse fluctuations of the laser system and instability in the mass-flow controllers at lower flow speeds.

3. Results and discussion

The digital delay generator permits temporal scanning of the laser diagnostic system with respect to the applied voltage pulses. This feature is utilized to determine NO population versus time delay from voltage onset for a given data condition. With this PLIF collection system, flame-produced NO populations are comparable to the detection noise threshold. For this reason a flame background image is collected in addition to the camera noise background image. However, plasma-produced NO populations are significantly higher and excited state NO emission is within the pass-band of the collection system. For each data point collected, both a plasma/flame only image and a plasma/flame/PLIF image are collected. Each raw image set is background subtracted to eliminate flame background and camera noise signals. Plasma/flame emission levels are then subtracted from the plasma/flame/PLIF images to leave only NO PLIF signal. Datasets presented below show both the corrected PLIF signal as well as the plasma emission for comparison.

Within a processed image, specific regions are integrated to determine total PLIF signal. Figure 4 shows the spatial layout of the imaged area with respect to the flame/anode and the three 0.5 mm × 0.5 mm regions of interest integrated. The first point (A in figure 4) is located directly under the anode and is where the NO PLIF emission as well as the NO plasma emission is the strongest. The second region of interest (B in figure 4) is below region of interest A while still within the discharge volume. This middle-of-the-plasma-volume location shows both strong PLIF and plasma emission, but is far enough away from the anode tip to allow the emission to be more spatially uniform and absent from strong gradients. Area B is displayed below, and most of the studies discussed below originate from area B unless otherwise noted. This area is selected because it is in the plasma discharge volume and it best shows the effect of the plasma on the flame, but is away from the tip of the anode where the strongest, non-uniform emissions are observed from plasma/PLIF. The third region of interest (C in figure 4) is located in the exhaust gas region and is sufficiently far away from the plasma volume so that no plasma emission is observed from the initial discharge. This location is selected to observe convection/diffusion effects downstream.

Figure 5 below shows typical corrected single-shot NO PLIF measurements with a false color scale collected at various time delays after the pulsed discharge. The anode is located at

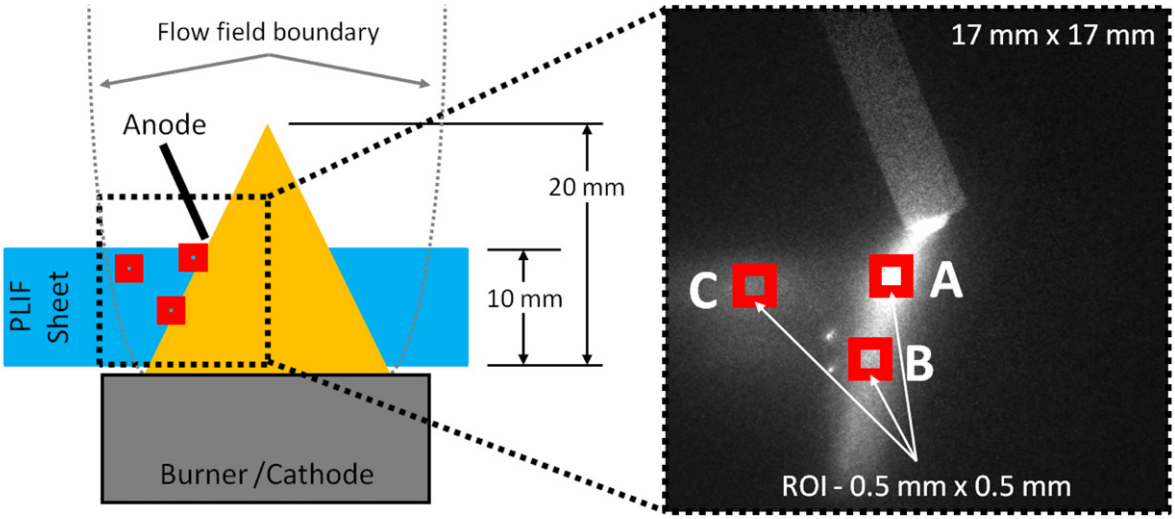

Figure 4. Spatial layout of anode/flame configuration with sample set of data. UV beam is passed under the anode and above the burner face to eliminate scatter. Thermal NO populations are augmented by plasma-produced NO (visible in the sample data image). Three specific locations (under anode (A), middle discharge (B), and exhaust gas (C)) within the image sets are used and integrated to find the total signal. Imaged region measures 20 mm by 20 mm.

the top of the image with the discharge striking downward to the grounded burner surface. Initially observed in this image sequence is the distribution of the NO fluorescence signal. Much larger signals are observed up to 2 mm from the anode compared to what is observed in the middle of the discharge. This variation is likely related to local temperature-driven density gradients in the plasma volume. As the gas density decreases with increased axial distance from the burner head pre-heat zone, the reduced electric field is increased. This thermally driven increase in reduced electric field strength near the anode allows for stronger electron impact excitation rates. To verify this, three important plasma species were selected (N_2, OH and O) and their emission was collected at various times after the discharge. These single-shot images are shown in the lower portion of figure 5. These emissions were collected in the same geometry as the NO PLIF images of the flame and appear not to be affected by the thermal fields. Initially, all three species show emission within the discharge volume that is relatively constant aside from the very near (less than 0.7 mm) electrode locations. These emission levels also show that the lifetime of the plasma discharge and the generated excited species are quite short with most of the collected emission decaying within 500 ns. It is suggested that while the excited states distribution is not affected, these thermal effects have a very large effect on the produced NO populations. The significantly increased temperature near the anode causes NO production to be greatly augmented and populations observed here are much larger due to a significantly higher reduced electric field in this lower gas density area compared to the pre-heat zone near the burner. The second item to be noted in the NO PLIF images is the convective transport of the NO populations that occurs. This is more evident in the larger time delays from the discharge. Between 25 and 100 μs the near anode populations are shown to spread downstream with the overall gas flow. While peak signal has decreased, the integrated signal from the larger area has only decayed by approximately 15%. The much larger 500 μs delay time shows

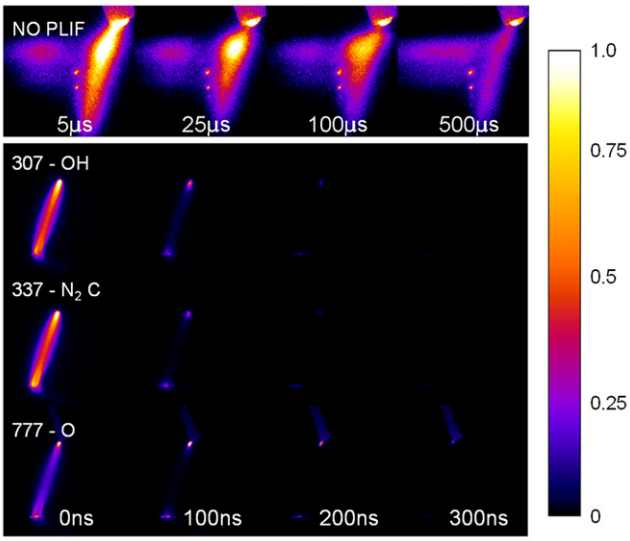

Figure 5. Typical single-shot, two-dimensional NO PLIF images at various delays from the discharge are shown at the top. Below are single-shot images of emission from various important combustion species produced by the discharge. The short lifetime provides an upper-bound of the lifetime of the discharge.

the final stages of the convective transport as it merges with the hot exhaust over 5 mm downstream.

Figure 6 shows NO radical density decay times versus delay from the onset of the voltage pulse for different applied voltages from the fast rise-time voltage pulse for a $\Phi = 0.80$ premixed, propane/air flame. The region of integrated PLIF signal displayed here from area B is shown in figure 4. The dashed line denoted by (P) in figure 6 show plasma emission whereas the solid lines show signal from NO PLIF denoted by (F). It is important to note that the plasma emission levels may not be an accurate measure of local NO concentration as optical emission relies greatly on spectral resolution, reduced electric field dependent electron impact excitation rates of NO excited

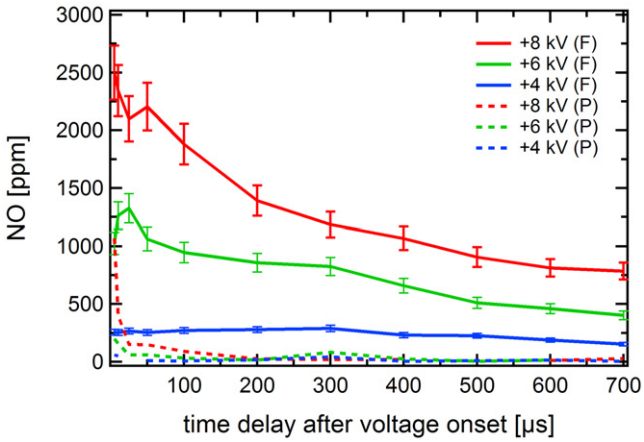

Figure 6. Decay rates of super-equilibrium NO produced in the middle of the plasma volume as a function of delay from the onset of applied voltage for three voltage levels for a $\Phi = 0.80$, propane/air flame. Solid lines represent corrected PLIF signals (F) and dashed lines show plasma emission only (P).

states and collisional quenching rates. Nonetheless, the PLIF signal has been corrected to remove this plasma emission as previously mentioned. As applied voltage levels are increased the initial production of NO in the middle of the discharge volume is also increased. This trend is observed in both NO signals; from plasma only and from NO PLIF. It is important to note that while plasma produced NO is distinguishable with this collection system, NO PLIF signal with the plasma on is sufficiently stronger compared to a condition with the plasma turned off. The condition with the highest applied voltage show peak NO concentrations of 2500 ppm. This is an increase of nearly two orders of magnitude over normal combustion produced NO and is similar to results observed in a corona-type discharge [20]. From both the plasma produced NO emission and also NO PLIF signals, it is possible to look at the decay of the super-equilibrium NO populations as the timing of the PLIF data acquisition is changed with the delay generator. The highly repeatable nature of this discharge is relied upon for consistency of the sequential measurements to build a stitched-temporal dataset. From this temporal evolution of NO signal it is possible to look at the decay rates of both the plasma and NO PLIF signals. The plasma emission shows a rapid decay of signal to the detection threshold level. This signal level appears to depend on the applied voltage level with a higher applied voltage level resulting in a higher signal level suggesting the long decay times of the plasma-produced NO cause a gradual build-up depending on the initial plasma-based production. The long decay times coupled with the local temperatures in excess of 1000 K suggest that diffusion of the produced NO could cause some of the decay behavior and must be considered. The +8 kV and +6 kV NO PLIF signals show very similar decay rates, especially after 250 μs, even though each started at a different initial super-equilibrium population providing a stronger case for NO radical density decay via diffusion.

A simple estimate of flow residence time within the volume of the discharge is performed to ensure that a volume of gas is only excited once. Based on the cold reactants flow speed of approximately 2 m s^{-1}, a volume of gas can move approximately 2 mm between 1 kHz discharges. If this volume of gas were to move entirely axially, multiple discharges could affect the same volume of gas. However, when these reactants undergo the thermal expansion across the reaction zone for this constant pressure combustion process, they accelerate and travel normal to the reaction zone. This acceleration to over 5 m s^{-1} [26] after thermal expansion of combustion combined with the narrow discharge volume occurring near the reaction zone, it is concluded that only a single discharge process occurs for a given volume of gas. However, diffusion occurring within this 1 mm timescale could cause the next volume of gas within the discharge to have artificially higher concentrations of NO due to pulse-to-pulse cumulative build-up.

The initial NO production during the plasma pulse can come from a variety of plasma-initiated sources. However, based on the previously listed pathways, reactant populations and related rates of reaction it is suggested that vitiated air-plasma chemistry is largely responsible for the large initial production of NO in the downstream region of the flame. While it is possible that combustion-related chemical reactions could be modified or augmented due to the additional energy of the pulsed plasma, these reactions are generally well-balanced in the high temperature region of the flame where the discharge occurs. In addition, the reaction rates with the newly formed, super-equilibrium products from discharge are typically larger than the combustion-based reaction rates; especially those involving vibrationally excited nitrogen or water vapor [27]. From this diagnostic alone, the results of the plasma-modified combustion reactions cannot be neglected, but are suggested to have minimal impact on local gas temperatures. The slow decay of the produced NO is another matter. The consumption of the super-equilibrium NO should more heavily rely on the reverse reactions of the combustion-related production mechanisms previously listed, specifically those from the thermal NO and N_2O mechanism, since there is no additional energy actively being deposited into the flame zone from the pulsed discharge. These reactions include equations (5)–(7), (13), (15) and (16). However, a relatively slow decay times longer than 700 μs suggest these reverse reactions are not significantly balancing the super-equilibrium NO produced by the pulsed discharge at a rate that would be useful for many combustion applications.

The zero dimensional CHEMKIN [32] code mentioned previously can be used to predict the equilibrium NO populations of a flame condition based on a known equivalence ratio for a burner-stabilized, premixed, propane/air flame. This code suggests that the NO mole fraction just past the reaction zone in the hot portions of the flame should be between 10^{-6} and 10^{-5}. Again, this thermal-equilibrium level cannot be measured with the current diagnostic system. Longer decay times than expected in thermal-equilibrium conditions combined with the minimum detectable signal levels and the CHEMKIN code calculation results suggest NO populations far above thermal equilibrium are augmented and maintained by the kHz repetition rate point-to-plane discharge in flame-vitiated air.

To better understand these chemical kinetics modifications, a similar test is performed by applying +8 kV for plasma

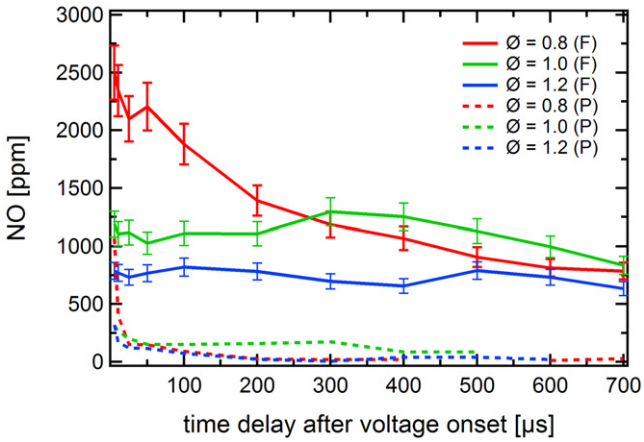

Figure 7. Decay rates of super-equilibrium NO produced in the middle of the plasma volume as a function of delay from the onset of applied voltage for three equivalence ratios. Solid lines represent corrected PLIF signals (F) and dashed lines show plasma emission only (P).

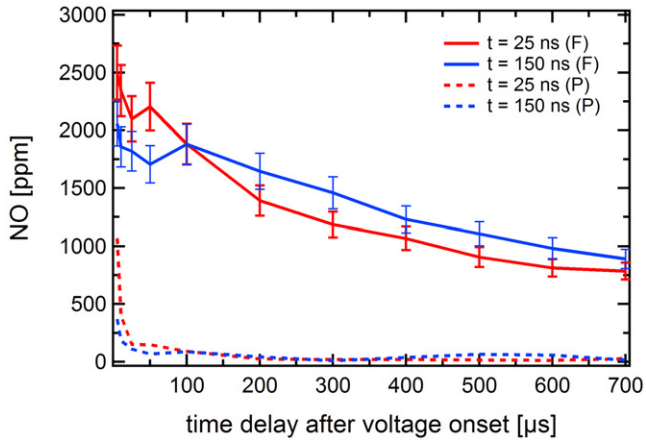

Figure 8. Decay rates of super-equilibrium NO produced in the middle of the plasma volume as a function of delay from the onset of applied shown for two different pulsers (25 and 150 ns voltage rise times) in a $\Phi = 0.80$ flame. Solid lines represent corrected PLIF signals (F) and dashed lines show plasma emission only (P).

generation in flames over a range of equivalence ratios. Overall equivalence ratios are varied from 0.8 to 1.2 and both plasma and NO PLIF emissions are collected for various delay times from the onset of the applied voltage to show how small deviations from unity can affect chemistry modification. With these small equivalence ratio changes, the total amount of electrical power that can be coupled to the flame is changed. This is likely due to a change in local temperature and a change in gas composition. The equivalence ratio of $\Phi = 1$ flame shows the highest power deposited at just over 15 W for a 1 kHz pulse repetition rate. The lean flame shows a 15% reduction from this level and the rich flame shows 23% reduction. Shown in figure 7 are initial build up and decay times of super-equilibrium populations in the middle of the plasma discharge recorded by delaying the collection system from the onset of the applied voltage. In all cases the NO PLIF emission is stronger than plasma emission which are still higher than thermal-equilibrium flame NO signal levels. The lean flame condition shows the greatest augmentation of both plasma and NO PLIF emission whereas minimal build-up or decays are shown for both the balanced and rich equivalence ratios since NO production is strongly dependent on the level of excess air for both equilibrium and non-equilibrium production/recombination mechanisms [24].

Results of the balanced and rich equivalence ratios suggest that even with sufficient levels of electrical power deposited in the flame, the flame chemistry is balanced such that NO radical density decay is unchanged.

A study of super-equilibrium NO production is performed to test the effectiveness of each pulser. Previous studies between these two types of pulsers on OH super-equilibrium production [25] has suggested that the faster rise-time voltage pulse is more efficient in super-equilibrium species production as measured by level of production per deposited plasma energy level. Utilizing the two optimum production conditions shown previously, the two pulsers are used to apply +8 kV to a premixed, propane/air flame with overall equivalence ratio of 0.8. Shown in figure 8 are the production and decays of NO for the two pulsers as a function of delay from the onset of the applied voltage. Unlike that previously seen with super-equilibrium OH, initial NO production levels, as obtained from NO PLIF, are very similar with the same energy deposited per pulse with each pulser. The change in voltage pulse rise time and therefore more rapid heating of the gas in the discharge volume seems to show minimal effects. In addition, decay rates of NO PLIF signal for both pulser configurations are quite similar. The largest difference between the two pulsers appears to be in the plasma emission. Initially, the faster rise-time pulser shows a greater level of super-equilibrium NO production. As dictated by the pass-band of the collection filters, this increase in signal could come from an excited state of NO (NO*) and could result due to the increased heating of the gas in the plasma discharge [41] and/or by direct electron impact production of NO*.

Lastly, other regions of interest are spatially averaged to observe the effects listed previously in figure 4. Effects at region of interest A in figure 4 are quite similar to those observed in region B and discussed above. The main differences being that initial production levels are as much as 25% higher than those of region B, but decay rates showed very similar trends as compared against time delay after onset of applied voltage, applied voltage level, equivalence ratio, and pulser configuration. Area C in figure 4 shows different behavior than A or B. This is due to the fact that area C is located out of the plasma discharge volume and does not directly see the effects from the energy deposited or the rapid thermal heating. Figure 9 shows the super-equilibrium NO emission levels for three different equivalence ratios. Minimal production is observed for all three equivalence ratios by either the plasma or the PLIF emission. Again, this can be attributed to the distance between the plasma volume and the sampling region. However, all three equivalence ratios show modification of the emission levels delayed in time by 500 μs from the onset of the applied voltage. Based on the local flow speeds of over 5 m s^{-1} [26] and the distance between the plasma and the region of interest, this agrees with initial super-equilibrium NO being produced in the plasma discharge

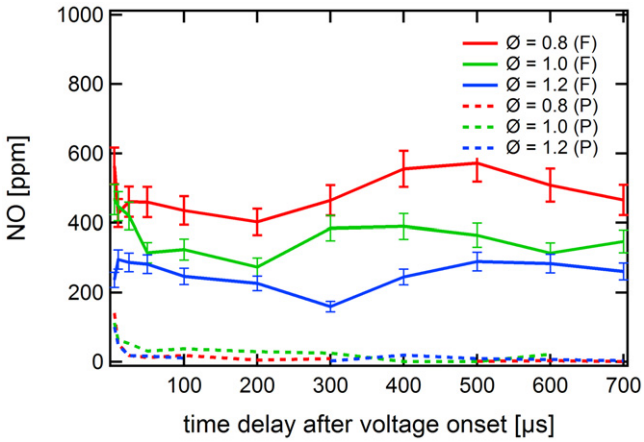

Figure 9. Decay rates of super-equilibrium NO produced in the exhaust gas as a function of delay from the onset of applied voltage for three equivalence ratios. Solid lines represent corrected PLIF signals (F) and dashed lines show plasma emission only (P).

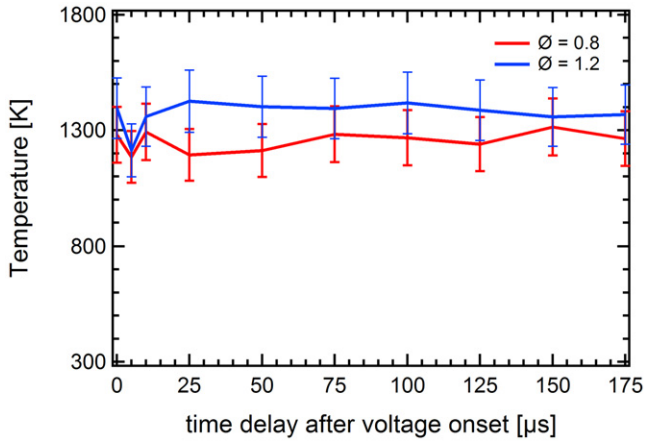

Figure 10. Point-based Raman scattering for temperature results. Region of interrogation is located 2 mm below the anode in the discharge volume.

volume (area B in figure 4) and being convected downstream with the local flow to area C. The lean equivalence ratio shows the strongest emission modification later in time while the rich equivalence ratio showing the weakest modification. This also agrees with the previous findings.

Point-based temperature measurements by spontaneous Raman scattering were conducted previously with this burner setup. This measurement, described in detail elsewhere [25], determines the ratio of total Stokes- and anti-Stokes-shifted signal in the first excited vibrational level to find temperature assuming a known number density and constant pressure of nitrogen. The collection volume that is approximately 0.1 mm^3 is located 2 mm below the anode in the discharge volume coinciding with the location of peak NO fluorescence signal. It was suspected that a significant increase in temperature in this location could cause a significant increase in NO production as well as slower decay times of the produced species. The results, displayed below in figure 10, show the temperatures recorded are significantly reduced from an adiabatic temperature expected at these equivalence ratios. This likely occurs for two reasons. The most significant reason is that this is a burner-stabilized flame which relies on a large thermal mass to help pre-heat the incoming premixed reactants to increase flame stability limits. The flame rejects large amounts of energy through standard transport processes to the burner head, especially at lower flow rates, which removes heat from the flame reducing the expected peak temperatures. Additionally, the point-based collection location is just outside the flame reaction zone, roughly halfway from the burner surface to the flame tip. Peak temperatures for a premixed conical flame occur closest to the tip of the flame and at this location the products have begun to form and cool. In addition to the reduced temperatures observed, the temporal evolution of temperature in this location is very stable. The only temporal behavior appearing in the plot occurs a few μs after the onset of discharge. This is most likely caused by a shockwave that is generated by the fast voltage rise time of the discharge causing small flame perturbations [25]. Outside of these behaviors, our results suggest that thermal effects induced from the plasma are not the suspected cause for this significant increase in NO production or slowed decay times.

4. Conclusion

In conclusion, we have shown that with approximately 15 mJ of electrical energy deposited in 2 cm^3 with a fast voltage rise-time (25 ns) pulser, we were able to produce nearly 100 times more than the thermally produced NO concentration in a premixed, propane/air flame. The largest production region is observed within 3 mm of the anode, but the plasma location is too far downstream from the pre-heat zone to have significant effect on the flame kinetics. The temporally stitched NO density measurements show a 50% density decay time lasting over 100 μs in downstream regions in the flame where gas temperatures are known to have exceeded the crossover temperature. Previously conducted point-based Raman temperature measurements suggest that increased thermal contributions from the pulsed discharge are not responsible for the increased NO number densities and reduced decay times observed. We conclude NO populations produced by the pulsed discharge are not consumed through reverse reaction mechanisms at rates fast enough to prevent a build-up of super-equilibrium NO. These significant NO radical populations last in the downstream region for over 700 μs and maybe subject to diffusion which would artificially increase decay rates. The larger portion of the discharge volume is in the post-reaction-zone of the flame and the largest NO production occurs downstream in a hot, low density region where the reduced electric field is higher than the colder pre-heat zone. This suggests the present plasma configuration producing large amounts of super-equilibrium NO is not the optimum for plasma-assisted combustion enhancement where hot *burnt gases* already exist. This configuration may be more favored for plasma-initiated ignition of fuel at reduced gas pressure since a large volume ignition kernel can be produced sufficiently far away from a surface.

Acknowledgments

Funding for this research was provided by the Air Force Office of Scientific Research (Dr. Jason Marshall, Program Manager) and by the Air Force Research Laboratory under Contract No. FA8650-10-C-2008.

References

[1] Kim W, Do H, Mungal G, and Capelli M A 2008 Optimal discharge placement in plasma-assisted combustion of a methane jet in cross flow *Combust. Flame* **153** 603–15

[2] Ahmed S F, Balachandran R, Marchione T, and Mastorakos E 2007 Spark ignition of turbulent nonpremixed bluff-body flames *Combust. Flame* **151** 366–85

[3] Pilla G, Galley D, Lacoste D A, Lacas F, Veynante D and Laux C O 2006 Stabilization of a turbulent premixed flame using a nanosecond repetitively pulsed plasma *IEEE Trans. Plasma Sci.* **34** 2471–7

[4] Pilla, G L, Lacoste D A, Veynante D, Laux C O 2008 Stabilization of a swirled propane–air flame using a nanosecond repetitively pulsed plasma *IEEE Trans. Plasma Sci.* **36** 940–1

[5] Cha M S, Lee S M, Kim K T and Chung S H 2005 Soot suppression by nonthermal plasma in coflow jet diffusion flames using a dielectric barrier discharge *Combust. Flame* **141** 438–47

[6] Criner K, Cessou A, Louiche J and Vervisch P 2006 Stabilization of turbulent lifted jet flames assisted by pulsed high voltage discharge *Combust. Flame* **144** 422–5

[7] Galley D, Pilla G, Lacoste D, Ducruix S, Lacas F, Veynante D and Laux C O 2005 Plasma-enhanced combustion of a lean premixed air–propane turbulent flame using a nanosecond repetitively pulsed plasma *43rd AIAA Aerospace Sciences Meeting and Exhibit (Reno, Nevada, USA, 10–13 January 2005)* AIAA-2005-1193

[8] Kim W, Do H, Mungal M G and Cappelli M A 2005 Parametric study of flame stabilization and NO production in a plasma assisted methane/air premixed flame *WSS/CI Fall Meeting (Stanford, CA)* 05F-78

[9] Kim W, Do H, Mungal M G and Cappelli M A 2007 *Proc. Combust. Inst.* **31** 3319–26

[10] Kim W, Mungal M G and Cappelli M A 2009 The role of in situ reforming in plasma enhanced ultra-lean premixed methane/air flames *Combust. Flame* **157** 374–83

[11] Kim Y, Ferreri V W, Rosocha L A, Anderson G K, Abbate S and Kim K 2006 Effect of plasma chemistry on activated propane/air flames *IEEE Trans. Plasma Sci.* **34** 2532–6

[12] Lou G, Bao A, Nishihara M, Keshav S, Utkin Y G and Adamovich I V 2006 Ignition of premixed hydrocarbon–air flows by repetitively pulsed, nanosecond pulse duration introduction plasma *41st AIAA Aerospace Sciences Meeting and Exhibit (Reno, Nevada, USA, 9–12 January 2003)* AIAA-2006-1215

[13] Mintoussov E I, Nikipelov A A, Starikovskaia S M and Starikovskii A Y 2006 Liquid fuel atomization and heterogeneous combustion of fuel-oxidizer mixtures using nanosecond discharge *44th AIAA Aerospace Sciences Meeting and Exhibit (Reno, Nevada, USA, 9–12 January 2006)* AIAA-2006-0614

[14] Ombrello T, Qin X, Ju Y, Gangoli S, Gutsol A and Fridman A 2006 Non-equilibrium plasma discharge: characterization and effect on ignition *44th AIAA Aerospace Sciences Meeting and Exhibit (Reno, Nevada, USA, 9–12 January 2003)* AIAA-2006-1214

[15] Pancheshnyi S, Lacoste D A, Bourdon A and Laux C O 2005 Propane–air mixture ignition by a sequence of nanosecond pulses *Proc. 1st European Conf. for Aerospace Sciences (EUCASS)(Moscow, Russia, 2005) 5-12-05*

[16] Starikovskaia S M, Anikin N B, Kosarev I N, Popov N A and Starikovskii A Y 2006 Analysis of ignition by nonequilibrium sources. Ignition of homological series of hydrocarbons by volume nanosecond discharge 44th *AIAA Aerospace Sciences Meeting and Exhibit (Reno, Nevada, USA, 9–12 January 2006)* AIAA-2006-0616

[17] Starikovskaia S M 2006 Plasma assisted ignition and combustion *J. Phys. D: Appl. Phys.* **39** R265–99

[18] Mintoussov E I, Pancheshnyi S V, and Starikovskii A Y 2004 Propane–air flame control by non-equilibrium low-temperature pulsed nanosecond barrier discharge *42nd AIAA Aerospace Sciences Meeting and Exhibit (Reno, Nevada, USA, 2004)* AIAA-2004-1013

[19] Adamovich I, Choi I, Jiang N, Kim J, Keshav S, Lempert W, Mintusov E, Nishihara M, Samimy M and Uddi M 2009 Plasma assisted ignition and high-speed flow control: non-thermal and thermal effects *Plasma Sources Sci. Technol.* **18** 034018

[20] Rao X, Matveev I B and Lee T 2009 Nitric oxide formation in a premixed flame with high-level plasma energy coupling *IEEE Trans. Plasma Sci.* **37** 2303–13

[21] Uddi M, Jiang N, Adamovich I V and Lempert W R 2009 Nitric oxide density measurements in air and air/fueld nanosecond pulse discharges by laser induced fluorescence *J. Phys. D: Appl. Phys.* **42** 075205

[22] Glassman I 1996 *Combustion* (New York: Academic)

[23] Law C K 2006 *Combustion Physics* (Cambridge: Cambridge University Press)

[24] Becker K H, Kogelschatz U, Schoenbach K H and Barker R J 2004 *Non-Equilibrium Air Plasmas at Atmospheric Pressure* (Boca Raton, FL: CRC Press)

[25] Schmidt J and Ganguly B 2012 Point-to-plane pulsed discharge initiated flame structure modification in propane–air flame *J. Phys. D. Appl. Phys.* **45** 045203

[26] Schmidt J, Kostka S, Roy S, Gord J and Ganguly B 2013 kHz-rate particle-image velocimetry of induced instability in premixed propane/air flame by millisecond pulsed current–voltage *Combust. Flame* **160** 276–84

[27] Burnette D, Shkurenkov I, Lempert W and Adamovich I 2013 *66th Annual Gaseous Electronics Conf.* (Princeton, NJ, USA, 30 September–4 October 2013) FT1 7

[28] Crosley D R 1980 *Laser Probes for Combustion Chemistry* (Washington, DC: American Chemical Society)

[29] Eckbreth A C 1996 *Laser Diagnostics for Combustion Temperature and Species* (Boca Raton, FL: CRC Press)

[30] Hanson R 1988 Combustion diagnostics: planar imaging techniques *Symp. (Int.) on Combustion/The Combustion Institute* vol 21, pp 1677–91

[31] Hanson R K and Salimian S 1984 Survey of rate constants in the N/H/O system *Combustion Chemistry* ed W C Gardner Jr (Berlin: Springer) pp 361–421 chapter 6

[32] 2007 CHEMKIN®, release 4.1.1, Reaction Design

[33] Piper L G and Cowles L M 1986 Einstein coefficients and transition moment variation for the NO($A\,^2\Sigma^+$–$X\,^2\Pi$) transition *J. Chem. Phys.* **85** 2419–22

[34] Imajo T, Shibuya K and Obi K 1987 Rotational energy transfer in the NO $A\,^2\Sigma^+$ ($v' = 0$) state with He and Ar *Chem. Phys. Lett.* **137** 139–43

[35] Drake M C and Ratcliffe J W 1993 High temperature quenching cross sections for nitric oxide laser-induced fluorescence measurements *J. Chem. Phys.* **98** 3850–65

[36] Paul P H, Gray J A, Durant Jr J L and Thoman Jr J W 1993 A model for temperature-dependant collisional quenching of NO $A^2\,\Sigma^+$ *Appl. Phys.* B **57** 249–59

[37] Paul P H, Gray J A, Durant Jr J L and Thoman Jr J W 1996 Collisional electronic quenching rates for NO $A^2\,\Sigma^+$ *Chem. Phys. Lett.* **259** 508–14

[38] Nee J B, Juan C Y, Hsu J Y, Yang J C and Chen W J 2004 The electronic quenching rates of NO ($A^2\,\Sigma^+$, $v' = 0$–2) *Chem. Phys.* **300** 85–92

[39] Settersten T B, Patterson B D and Gray J A 2006 Temperature-and species-dependent quenching of NO $A^2\,\Sigma^+$ ($v' = 0$) probed by two-photon laser-induced fluorescence using a picosecond laser *J. Chem. Phys.* **124** 234308

[40] Luque J and Crosley D R 1999 LIFBASE: Database and spectral simulation (version 2.1.1) *SRI International Report* MP 99-009

[41] Starikovskii A, Nudnova M, Kindusheva S and Aleksahdrov N 2010 Rate of plasma thermalization of pulsed nanosecond surface dielectric barrier discharge *48th AIAA Aerospace Sciences Meeting and Exhibit (Orlando, FL, USA, 4–7 January 2010)* AIAA-2010-0465